Phase-field model for mesoscale simulation of crystallization morphology evolution in 3D printing of thermoplastic composite

Siqin Liu[a], Chenguang Liang[b], Li-Hua Shao[c], Min Yi[b,*], Xin Yan[a,*], Wuxiang Zhang[a,d], Xilun Ding[a,d]

[a]*School of Mechanical Engineering and Automatic, Beihang University, Beijing, 100191, China*
[b]*State Key Laboratory of Mechanics and Control for Aerospace Structures & College of Aerospace Engineering, Nanjing University of Aeronautics and Astronautics, Nanjing, 210016, China*
[c]*Institute of Solid Mechanics, School of Aeronautic Science and Engineering, Beihang University, Beijing, 100191, China*
[d]*Ningbo Institute of Technology, Beihang University, Ningbo, 315832, China*

Abstract

3D printing has enabled the production of continuous fiber-reinforced thermoplastic composites (CFRTPCs) with exceptional mechanical properties and design flexibility. The crystalline morphological evolution during 3D printing of CFRTPCs, particularly the transcrystalline layer (TCL) that is critical for the mechanical performance, remains poorly modeled and understood. Herein, we develop a non-isothermal phase-field model (PFM) for mesoscale simulating the crystallization process and morphology evolution during the 3D printing of thermoplastic composites. The PFM is derived by constructing a free energy density functional incorporating order parameters to characterize the crystallization process, with the phase-field evolution equations being intrinsically coupled to heat transfer. In particular, the fiber-crystalline melt contact angle-dependent sporadic nucleation processes are integrated into the PFM using an explicit nucleation algorithm. Phase-field simulations of crystallization behavior in isotactic polypropylene (iPP) under conditions emulating 3D printing are demonstrated to verify the PFM capability. The influence of contact angle (θ), convective coefficient (h), and fiber spacing (D) on non-isothermal crystallization is comprehensively examined. It is found that TCL thickness increases with decreasing θ, smaller h, and larger D, until it reaches saturation. Slower cooling during 3D printing could significantly amplify the effects of both contact angle and fiber spacing on the TCL evolution. The proposed PFM could enable mesoscale simulation of 3D-printed thermoplastics and help optimization of crystallization and printing parameters.

Keywords: thermoplastic composites, 3D printing, transcrystalline layer, phase-field

*Corresponding author
Email addresses: yimin@nuaa.edu.cn (Min Yi), xin_yan@buaa.edu.cn (Xin Yan)

1. Introduction

Continuous fiber-reinforced thermoplastic composites (CFRTPCs) have garnered significant attention in industrial applications for their exceptional performance such as light weight, high strength, excellent toughness, and recyclability [1–3]. These composites can be manufactured by fused deposition modeling (FDM), a 3D printing technique known for its cost-effectiveness and ability to produce complex and intricately shaped components [4–7].

During the FDM process of CFRTPCs, the thermoplastic polymer undergoes solidification and forms its ultimate microstructure that is pivotal to the mechanical properties and geometric precision of the printed object [4–7]. For semicrystalline thermoplastic composites, the situation becomes even more complicated due to the polymer crystallization and the interactions between fibers and polymer matrix [7, 8]. In composites, the introduction of reinforcing fibers in thermoplastic may lead to the formation of a special columnar structure on the fiber surface, known as the transcrystalline layer (TCL) [9]. The TCL structure has been reported to significantly influence the mechanical properties of the fiber-reinforced composites [10, 11]. Specifically, it affects the interfacial adhesion between fibers and polymer matrix [12–16], as well as the matrix properties such as Young's modulus [17–19] and thermal expansion coefficient [13]. Furthermore, the TCL feature — including its morphology and fraction — is highly dependent on processing parameters such as printing temperature and fiber distribution [3, 7]. A comprehensive modeling and understanding of the underlying mechanisms are essential for effectively controlling TCL formation. Nevertheless, because of the microscale nature of the crystalline structures, real-time monitoring of the TCL growth during 3D printing remains a challenge. Current experimental studies primarily focus on the relationships between the final TCL morphology and various factors [10, 11, 20] such as thermal conditions [21] and fiber surface properties [16, 22]. However, these studies fail to fully capture and understand the polymer crystallization behavior and its mechanism during 3D printing process, and even sometimes achieve conflicting results. For example, Moon et al. find an inverse relationship between TCL thickness and fiber diameter [23], while Pompe and Maeder demonstrate that TCL thickness is independent of fiber size [22]. Thus, a more systematic investigation on the polymer crystalline evolution during 3D printing is essential for controlling TCL structure and composite properties.

Computational modeling provides an effective approach for characterizing polymer crystalline morphology evolution during cooling process, but it is non-trivial. Numerous macroscale models have been developed to predict the evolution of crystallinity and the TCL thickness in composites by employing crystallization kinetics equations [24, 25]. However, these models fail to capture the detailed morphology of crystalline structures, including the boundaries between crystalline grains, which are crucial to the composites' fracture performance [10]. Several mesoscale

models, such as the pixel coloring method, offer the ability to simulate the crystalline morphology in composites during the tow-placement process [26], in short fiber-reinforced composites under non-isothermal conditions [27], and in thin-film polymer with transcrystalline [28]. However, these studies are primarily developed by using the phenomenological or mathematical nucleation and crystalline growth kinetics, but suffer from a lack a of thermodynamic or physical basis. This makes it challenging to describe phenomena such as void evolution and mesoscale heat transfer during 3D printing. Recently, the phase-field method, which employs thermodynamically consistent energy functionals to model microstructure evolution [29], has gained significant attention as a powerful computational tool for simulating material behaviors in 3D printing processes, including sintering, remelting, and solidification phenomena [30–34]. This method demonstrates great advantages in modeling complex interface dynamics without requiring explicit interface tracking [29], making it particularly valuable for investigating the non-equilibrium crystallization dynamics in thermoplastic composites under 3D printing conditions. However, a phase-field in this regards is still missing.

In this paper, we develop a non-isothermal phase-field model (PFM) for exploring the crystallization morphology evolution (in particular, TCL formation) during the solidification stage of FDM. The isotactic polypropylene (iPP) composite is selected as the model material, which has extensive applications in industry [35] and is frequently used for both experimental and numerical studies of TCL [15, 17, 36, 37]. The mechanisms governing TCL development are elaborated through the examination of various factors including fiber surface characteristics, temperature conditions, and fiber spacing. It is anticipated that the PFM could provide valuable insights for optimizing the crystalline microstructure and thus enhancing the printing quality and process efficiency of CFRTPCs.

2. Non-isothermal phase-field model

In this section, we firstly introduce the model set up and phase-field order parameters (OPs) that describe different phases during the crystallization morphology evolution in 3D printing. Then the PFM total free energy in terms of OPs is constructed. Subsequently, a series of phase-field dynamic equations and temperature evolution equation are formulated to describe the crystallization process. Finally, the incorporation of polymer nucleation and crystalline growth into PFM is presented.

2.1. Model setup and order parameters

A two-dimensional microscale PFM is established to investigate the crystallization behavior of iPP composites during the FDM process. The physical configuration of the FDM process is

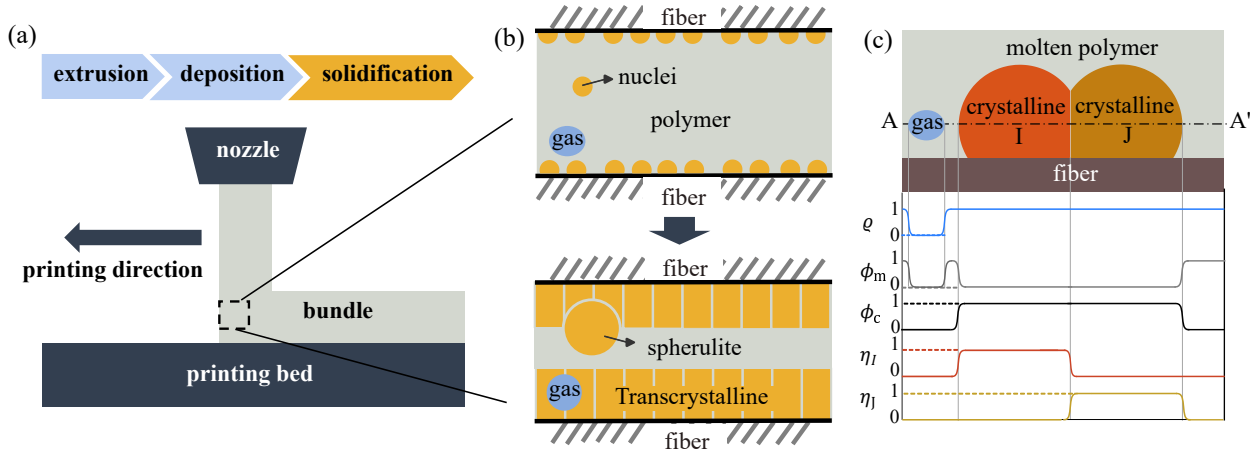

Fig. 1. Schematic representation of (a) FDM process, (b) crystalline structures, and (c) order parameter profiles across the A-A' section

illustrated in Fig. 1(a). In this process, polymer crystallization occurs after the material is extruded and deposited on the printing bed, where the temperature cools down below the melting point. In the crystallization simulation, a representative small square region within the printing bundle is selected to model the material behavior. This small region is placed between two neighboring fibers, allowing us to examine the TCL development on the fiber surface as well as the spherulites within the interior polymer, as depicted in Fig. 1(b). Our model primarily focuses on the evolution of crystalline grains, while the details of the crystallographic orientation are not considered in this work and the readers can refer to the PFM in [38–42] for such details.

In our PFM, different phases are represented by order parameters. The polymer crystalline and molten states are characterized by the non-conserved OPs ϕ_c and ϕ_m, respectively. The crystalline phase ϕ_c and molten phase ϕ_m take the value of unity within their corresponding phase and zero otherwise. The regions where OP values smoothly transition from 0 to 1 indicate the diffuse-interface between different phases. Additionally, the conserved OP ϱ distinguishes between material substance ($\varrho = 1$) and void/gas state ($\varrho = 0$). The OPs ϕ_c, ϕ_m and ϱ are constrained to satisfy $\phi_c + \phi_m = \varrho$, ensuring mass conservation of the material. Therefore, all subsequent mentions of ϕ_m can be replaced by $\varrho - \phi_c$ to reduce the number of unknown variables. Within the crystalline phase, the non-conserved OPs $\{\eta_i\}$ ($i = 1, 2, ...N$) are introduced to distinguish the individual growth of various crystalline grains. In a distinct crystalline grain, only one of the η_i values is unity, while the remaining η_i values are zero. The sum of all η_i values should fulfill the equation $\sum_{i=1}^{N} \eta_i = \phi_c$. We considered a toy structure comprising two crystalline grains, I and J, embedded within a polymer matrix ($\varrho = 1$). The corresponding OPs vary along the A-A' section, as depicted in Fig. 1 (c). The OPs ϕ_c and ϕ_m satisfy the relationship $\phi_c + \phi_m = \varrho$, while η_I and η_J

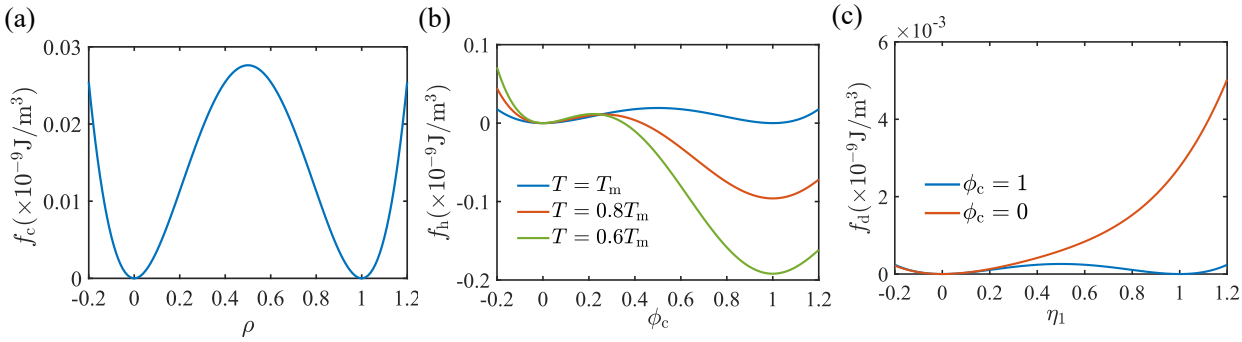

Fig. 2. (a) Depictions of the local free energy density contribution $f_c(0.8T_m, \varrho)$ as a function of ϱ, as formulated in Eq. (3); (b) Depictions of the local free energy density contribution $f_h(T, \phi_c, \phi_m = 1 - \phi_c, \varrho = 1)$ as a function of ϕ_c at temperatures $T = T_m, 0.8T_m$, and $0.6T_m$, as formulated in Eq. (6); (c) Depictions of the local energy density contribution $f_d(0.8T_m, \phi_c, \eta_1, \phi_c - \eta_1)$ as a function of η_1 when $\phi_c = 1$ and 0, as formulated in Eq. (7).

satisfy $\eta_I + \eta_J = \phi_c$.

2.2. *Free energy*

The total free energy density of the system is formulated as:

$$f = f_{loc}(\varrho, \{\eta_i\}, \phi_c, \phi_m, T) + \frac{1}{2}k_\varrho(T)|\nabla\varrho|^2 + \frac{1}{2}k_\eta(T)\sum_{i=1}^{N}|\nabla\eta_i|^2 + \frac{1}{2}k_c(T)|\nabla\phi_c|^2 + \frac{1}{2}k_m(T)|\nabla\phi_m|^2 \quad (1)$$

where f_{loc} represents the local Helmholtz free energy density and is a function of the OPs (ϕ_c, ϕ_m, ϱ, and $\{\eta_i\}$) and the temperature T; the last four terms represent the gradient energy corresponding to the respective OPs, k_η, k_c, k_m and k_ϱ represent the respective gradient energy coefficients. Here, the expression of f_{loc} is decomposed into four parts, i.e.,

$$f_{loc} = f_c(T, \varrho) + f_h(T, \varrho, \phi_c, \phi_m) + f_d(T, \phi_c, \{\eta_i\}) + f_{pt}(\{\eta_i\}). \quad (2)$$

The first part f_c embodies a double-well potential features two equilibrium states corresponding to the void/gas phase ($\varrho = 0$) and the material substance phase ($\varrho = 1$), as depicted in Fig. 2(a), which is constructed as

$$f_c = W_c(T)\varrho^2(1-\varrho)^2, \quad (3)$$

where W_c refers to the energy barrier between the two minimum states.

The second term, f_h, describes the phase transition between crystalline (ϕ_c) and molten (ϕ_m) phases, and consists of two components, i.e.,

$$f_h = f_{hc}(\varrho, \phi_c, \phi_m) + f_{ht}(T, \phi_c). \quad (4)$$

Here, f_{hc} represents the non-thermal energy contribution to the phase transition, while f_{ht} incorporates temperature-dependent effects. The term f_{hc} is formulated as

$$f_{\mathrm{hc}} = W_{\mathrm{h}}(T)\left\{\varrho^2 + 6(1-\varrho)\left[\phi_{\mathrm{c}}^2 + \phi_{\mathrm{m}}^2\right] - 4(2-\varrho)\left[\phi_{\mathrm{c}}^3 + \phi_{\mathrm{m}}^3\right] + 3\left[\phi_{\mathrm{c}}^2 + \phi_{\mathrm{m}}^2\right]^2\right\}, \tag{5}$$

which uses the form of a double-well function with two minima representing equilibrium states: the molten phase ($\phi_{\mathrm{c}} = 0$) and the crystalline phase ($\phi_{\mathrm{c}} = 1$), subject to the constraint $\varrho = \phi_{\mathrm{c}} + \phi_{\mathrm{m}}$. The parameter W_{h} determines the energy barrier height between these minima. The second portion f_{ht} in f_{h} represents the pure thermal effects, including the influence of the local temperature variation and the release or absorption of the latent heat, which is formulated as

$$f_{\mathrm{ht}} = \rho(\varrho)c_{\mathrm{p}}(\varrho)T\ln T + k_{\mathrm{ht}}\left(\frac{T}{T_{\mathrm{m}}} - 1\right)\mathscr{L}\Phi(\phi_{\mathrm{c}})\Phi(\varrho), \tag{6}$$

where ρ is the density, c_{p} is the specific heat capacity, T_{m} is the equilibrium melting point. $\mathscr{L}$ denotes the latent fusion of iPP polymer and serves as the driving force for crystallization, k_{ht} is a scalar energy coefficient that modulates the intensity of the crystallization driving force during the simulation. $\Phi(\phi_{\mathrm{c}})$ and $\Phi(\varrho)$ are the interpolation functions of ϕ_{c} and ϱ, respectively, satisfying the conditions $\Phi(X = 1) = 1$ and $\Phi(X = 0) = 0$ for $X = \phi_{\mathrm{c}}$ and ϱ. Given these properties and $\varrho = 1$, we can plot the profile of f_{h} as illustrated in Fig. 2(b). The blue line corresponds to the case where $T = T_{\mathrm{m}}$, exhibiting a double-well structure with two minima at zero. This indicates the coexistence of stable molten and crystalline phases. The orange and yellow lines represent scenarios where the temperature is below the melting point ($T < T_{\mathrm{m}}$). In these cases, the free energy density within the crystalline phase ($\phi_{\mathrm{c}} = 1$) remains lower than that within the molten phase ($\phi_{\mathrm{c}} = 0$), thereby promoting spontaneous solidification. Specifically, the temperature in the yellow line ($T = 0.6T_{\mathrm{m}}$) is lower than that in the orange line ($T = 0.8T_{\mathrm{m}}$), resulting in a more pronounced drop in f_{ht} when $\phi_{\mathrm{c}} = 1$. Consequently, the local free energy f_{h} of the crystalline phase decreases with lower temperatures, while the energy of the molten phase remains unchanged. This enhances the thermodynamic driving force for the transition from the molten to the crystalline state. In contrast, in the void/gas phase ($\varrho = 0$), such a transition does not exist. To ensure these behaviors, $\Phi(X)$ is typically given by $X^3(10 - 15X + 6X^2)$ for $X = \phi_{\mathrm{c}}$ and ϱ [43].

The f_{d} in Eq. (2) describes the growth of distinct crystalline grains within the polymer matrix, which is expressed as

$$f_{\mathrm{d}} = W_{\mathrm{d}}(T)\left[\phi_{\mathrm{c}}^2 + 6(1-\phi_{\mathrm{c}})\sum_{i=1}^{N}\eta_i^2 - 4(2-\phi_{\mathrm{c}})\sum_{i=1}^{N}\eta_i^3 + 3\left(\sum_{i=1}^{N}\eta_i^2\right)^2\right]. \tag{7}$$

This expression is formulated as a Landau-type polynomial [43], which enables the system to occupy multiple minimum states corresponding to various crystalline grains. The parameter W_{d}

correlates with the energy barrier height separating these local energy minima. Within the crystalline phase ($\phi_c = 1$), the set of order parameters $\{\eta_i\}$ ($i = 1, 2, ...N$) reaches equilibrium states. In each crystalline grain, only one of the η_i equals one, while the remaining η_i values are zero. In contrast, within the molten phase ($\phi_c = 0$), all the OPs $\{\eta_i\}$ are zero, signifying the absence of crystalline grains. Considering the toy structure illustrated in Fig. 1(c) with two crystalline grains ($N = 2$), the profile of f_d is depicted in Fig. 2(c). In crystalline region ($\phi_c = 1$, blue line), the system occupies either state in crystalline grain I ($\eta_I = 1, \eta_J = 0$) or in crystalline grain J ($\eta_J = 1, \eta_I = 0$), forming a bistable energy landscape. In molten regions ($\phi_c = 0$, orange line), the free energy minimum resides at ($\eta_I = \eta_J = 0$), with crystalline configurations ($\eta_I = 1$ or $\eta_J = 1$) energetically unfavorable.

Finally, a penalty term f_{pt} is incorporated into f_{loc} in Eq. (2) to describe the impingement among various crystalline grains [44] and is formulated as

$$f_{pt} = k_{pt} \sum_{i \neq j} \left(\eta_i^2 \eta_j^2 \right), \tag{8}$$

where the coefficient k_{pt} scales the effect of the penalty term throughout the simulation. Before impingement, the term $\eta_i^2 \eta_j^2$ is zero, allowing the expansion of crystalline grains. When grains come into contact with each other, $\eta_i^2 \eta_j^2$ takes on non-zero values at the boundaries, thereby hindering the further development of these grains.

2.3. *Evolution equations*

The evolution of the conserved OP ϱ is governed by the Cahn–Hillard equation [29] as

$$\frac{\partial \varrho}{\partial t} = \nabla \cdot \left[M(T) \nabla \left(\frac{\delta \int_\Omega f \mathrm{d}V}{\delta \varrho} \right) \right] = \nabla \cdot \left[M(T) \nabla \left(\frac{\partial f_{loc}}{\partial \varrho} - \nabla \cdot (k_\varrho \nabla \varrho) - \nabla \cdot (k_m \nabla (\varrho - \phi_c)) \right) \right], \tag{9}$$

where M represents the mobility coefficient that controls mass diffusion and reduces with decreasing temperature.

The dynamic evolution of the crystalline phase ϕ_c is governed by the Allen–Cahn equation [29] as

$$\frac{\partial \phi_c}{\partial t} = -L_\phi(T) \frac{\delta \int_\Omega f \mathrm{d}V}{\delta \phi_c} = -L_\phi(T) \left[\frac{\partial f_{loc}}{\partial \phi_c} - \nabla \cdot (k_c \nabla \phi_c) + \nabla \cdot (k_m \nabla (\varrho - \phi_c)) \right], \tag{10}$$

where L_ϕ is the kinetic coefficient that governs the growth rate of the crystalline phase during the simulation. It is determined to align with the crystalline growth rate proposed in [45] for iPP polymer, as further detailed in Sec. 2.4.

Furthermore, the evolution of various crystalline grains represented by η_i is also governed by the Allen–Cahn equation [29] as

$$\frac{\partial \eta_i}{\partial t} = -L_\eta(T)\left[\frac{\partial f_{\mathrm{loc}}}{\partial \eta_i} - \nabla \cdot (k_\eta \nabla \eta_i)\right], \tag{11}$$

$$L_\eta(T) = \widetilde{k} L_\phi(T), \tag{12}$$

where L_η is the kinetic coefficient and is related to L_ϕ through a multiplicative coefficient $\widetilde{k}$, which ensures kinematic consistency between crystalline growth rates for η_i and crystalline front propagation for ϕ_{c}.

The crystallization behavior of composites is profoundly influenced by the temperature field, which is closely related to the variation of internal energy density u [43]. This relationship can be described as

$$\frac{\partial u}{\partial t} = \nabla \cdot (k_T(\varrho) \nabla T)\,, \tag{13}$$

where $k_T(\varrho)$ denotes the thermal conductivity of the material. The internal energy density u is derived from Eq. (2), as detailed in the supplementary material Note 1. It is given by the following expression:

$$u = f_{\mathrm{loc}} - T\left(\frac{\partial f_{\mathrm{loc}}}{\partial T}\right)_V = u\left(T, \varrho, \phi_{\mathrm{c}}, \phi_{\mathrm{m}}, \sum_{i=1}^{N} \eta_i\right). \tag{14}$$

By applying the chain rule of differentiation, the left-hand side of Eq. (13) can be expanded as

$$\frac{\partial u}{\partial t} = \frac{\partial u}{\partial T} \cdot \frac{\partial T}{\partial t} + \frac{\partial u}{\partial \varrho} \cdot \frac{\partial \varrho}{\partial t} + \frac{\partial u}{\partial \phi_{\mathrm{c}}} \cdot \frac{\partial \phi_{\mathrm{c}}}{\partial t} + \frac{\partial u}{\partial \phi_{\mathrm{m}}} \cdot \frac{\partial \phi_{\mathrm{m}}}{\partial t} + \sum_{i=1}^{N}\left(\frac{\partial u}{\partial \eta_i} \cdot \frac{\partial \eta_i}{\partial t}\right). \tag{15}$$

2.4. Nucleation and crystalline growth

In our simulation, we consider the intermittent formation of nuclei within the polymer matrix, a process known as the sporadic nucleation [28]. This scenario is particularly pronounced under slow cooling conditions, where it takes a duration for the nuclei count to reach saturation. Herein, we incorporate the sporadic nucleation into our PFM.

In the current model, the sporadic formation of nuclei is modeled through an explicit nucleation method [46]. This method begins by selecting a random position in the simulation domain. Then the nucleation rate I, which refers to the number of nuclei formed per unit area and per unit time, is calculated for each position. The expression of I is given by

$$I(\phi_{\mathrm{c}}, \varrho, T, \theta) = I_{\mathrm{t}}(T, \theta) S(\phi_{\mathrm{c}}) \Phi(\varrho). \tag{16}$$

Here, I_{t} denotes the theoretical nucleation rate and is written as [47]

$$I_{\mathrm{t}}(T, \theta) = I_0 \exp\left[-\frac{U^*}{R(T - T_g^\infty)}\right] \exp\left[-\frac{A(\theta)}{T(T_{\mathrm{m}} - T)^2}\right]. \tag{17}$$

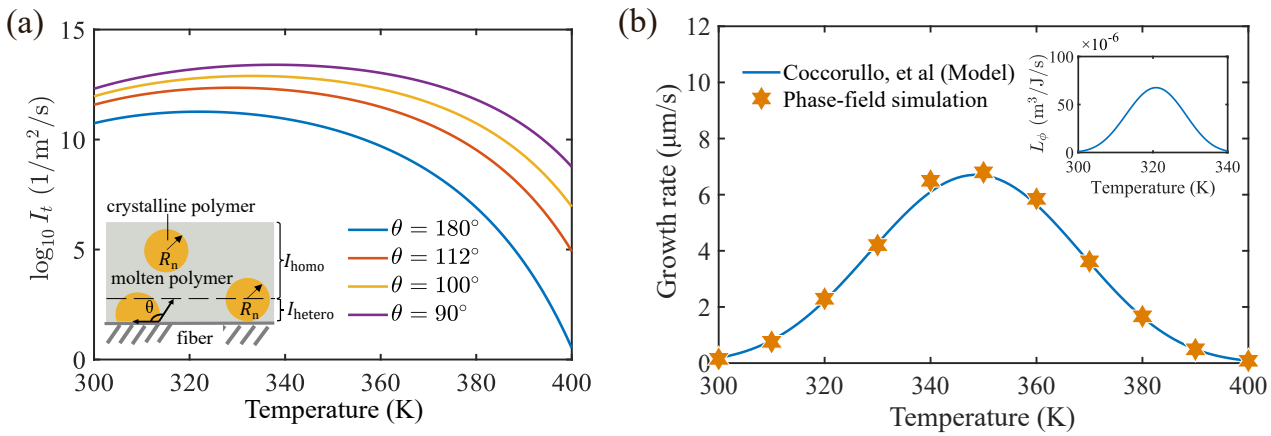

Fig. 3. (a) Nucleation rate as a function of temperature T under various contact angle θ. Inset: Description of the nucleation process. θ is contact angle at the fiber-crystalline-melt interface. The polymer region is delineated into two distinct areas: homogeneous nucleation region characterized by $I = I_{\text{homo}}$ and the heterogeneous nucleation region with $I = I_{\text{hetero}}$ which is influenced by the fiber surface. R_{n} refer to the predetermined radii of the nuclei; (b) Comparative evaluation of crystal growth rates between the simulation results obtained from our PFM and the model proposed by [45]. Inset: Plot of L_ϕ in Eq. (10) as a function of the temperature

where T is the crystallization temperature, θ is the contact angle at the fiber-crystalline-melt interface [47, 48], as illustrated in the schematic inset of Fig. 3(a). I_0 is the pre-exponential factor representing the theoretical maximum nucleation rate, U^* is the activation energy for the diffusion of crystallizing segments across the phase interface, R is the gas constant, T_g^∞ is the temperature where the crystallization ceases. The function $A(\theta)$ determines the energy barrier for critical nucleus formation and is expressed as

$$A(\theta) = A_0 \left(\frac{\theta - \frac{1}{2}\sin 2\theta}{\pi} \right), \tag{18}$$

where A_0 is a constant that represents the properties of homogeneous nucleation. As θ decreases, the nucleation energy barrier diminishes, leading to a reduction of $A(\theta)$ and consequently an increase in nucleation rate I_{t}, as depicted in Fig. 3(a). As θ approaches 0, the nucleation barrier vanishes, resulting in complete wetting of the crystalline on the fiber surface ($I_{\text{t}} = \infty$). Conversely, when θ approaches π, the homogeneous nucleation barrier is recovered. In our simulation, as shown in the inset of Fig. 3(a), the nucleation rate in the vicinity of the fiber surface is determined by $I_{\text{t}}^{\text{hetero}} = I_{\text{t}}(T, \theta_{\text{f}})$, where θ_{f} is the contact angle determined by the fiber characteristics. The depth of the fiber vicinity is set to match the predefined radius of the nuclei, thereby ensuring that any newly formed nucleus within this region comes into contact with the fiber surface. Meanwhile, in areas remote from the fiber surface, the nucleation rate equals $I_{\text{t}}^{\text{homo}} = I_{\text{t}}(T, \pi)$, signifying the mechanism of homogeneous nucleation. Additionally, we implement an algorithm to prevent

nucleation in the regions that already crystallized. This algorithm is incorporated into the term $S(\phi_c)$ in Eq. (16), as detailed in Supplementary Material Note 2. We also use the interpolation function $\Phi(\varrho)$ (defined in Eq. (6)) to prevent nucleation within the void/gas phase ($\varrho = 0$). After the nucleation rate I is determined, the nucleation probability P is calculated using the formula

$$P = 1 - \exp(-I\Delta T), \tag{19}$$

where $\Delta T = T_m - T$ is the undercooling. Subsequently, a random number uniformly distributed between 0 and 1 is generated. If this number is less than P, a nucleus with a predetermined radius R_n will be introduced into the system.

After being introduced into the system, the nuclei would expand at a temperature-dependent rate in their radial direction, known as the linear growth rate of the crystalline structure. In this model, the growth rate is governed by the dynamic coefficient L_ϕ in Eq. (10), which is given by:

$$L_\phi(T) = a_1 \exp\left(\frac{-a_2}{T - T_g^\infty}\right) \exp\left(\frac{-a_3}{T_m - T}\right), \tag{20}$$

where a_1, a_2, and a_3 are the constant coefficients. These coefficients are determined to compare the simulated crystalline growth rate obtained from our model (orange markers) with the theoretical model proposed in reference [45] (blue line) for iPP polymer, as illustrated in Fig. 3(b). In our subsequent simulations, the coefficients a_1, a_2, and a_3 are employed and remain unchanged.

Furthermore, an advanced algorithm for the dynamic allocation and reassignment of the OPs $\{\eta_i\}$ has been integrated into the simulation processes of crystalline nucleation and growth. This algorithm aims to minimize the number of OPs necessary to differentiate the multiple crystalline grains. Comprehensive details regarding the implementation and execution of this algorithm can be found in reference [43, 49].

3. Determination of model parameters

The material and PFM paramters utilized in this simulation are presented in Table 1. The properties ρ_{ipp}, k_T^{ipp}, and c_p^{ipp} represent the density, thermal conductivity, and heat capacity at constant pressure for iPP ($\varrho = 1$), respectively. ρ_g, k_T^g, and c_p^g represent the same properties for air ($\varrho = 0$). I_0 in Eq. (17) is fitted so that the nucleation density of pure iPP polymer at 380 K in the PFM simulation matches that of the model in reference [45]. Additionally, the coefficient k_{ht} in Eq. (6), which is a tunable parameter that modulates the driving force for crystallization within the simulation, is set to 3×10^{-3} to achieve stable simulation behavior.

The local energy parameters $W_c(T)$, $W_h(T)$, and $W_d(T)$, along with the gradient energy parameters $k_\varrho(T)$, $k_\eta(T)$, $k_c(T)$, and $k_m(T)$ in Eqs. (1) to (8), are determined by fitting to the interfacial

energies γ_{mg}, γ_{cg}, γ_{mc}, and γ_{gb}, which represent the polymer melt/gas, polymer crystalline/gas, polymer melt/polymer crystalline, and grain boundaries interfaces, respectively [50]. Here, γ_{cg} is correlated with γ_{mg} according to the formula [50]

$$\gamma_{cg} = \left(\frac{\rho_c}{\rho_a}\right)^{\beta} \gamma_{mg} = \left(\frac{0.94}{0.85}\right)^{1.3} \gamma_{mg} = 1.38\gamma_{mg}, \tag{21}$$

where ρ_c represents the crystalline density, ρ_a is the melt density, and β is Macleod's coefficient. Then γ_{mc} is estimated as [51, 52]

$$\gamma_{mc} = \gamma_{cg} + \gamma_{mg} - 2\psi_{cl}\sqrt{\gamma_{cg}\gamma_{mg}}. \tag{22}$$

The constant ψ_{cl} characterizes the interfacial interaction between crystalline and melt polymer molecules. It is assumed to be uniform for the same type of polymer.

Table 1. Material and PFM parameters used in this simulation [45, 47, 50, 53]

Parameters	Units	Values	Parameters	Units	Values
ρ_{ipp}	kg/m^3	0.9×10^3	k_T^{ipp}	W/m/K	0.17
c_p^{ipp}	J/K/kg	1800	ρ_g	kg/m^3	1.23
k_T^g	W/m/K	0.025	c_p^g	J/K/kg	1006
T_m	K	460.7	$\mathscr{L}$	J/m^3	1.6×10^8
U^*	cal/mol	1500	R	J/mol/K	8.314
T_g^∞	K	236	A_0	K^3	1.78×10^7
I_0	1/m^2/s	1×10^{19}	M	m^2/J/s	$20 \tanh\left(\frac{T-340}{80}\right)$
a_1	m^3/J/s	9.05×10^2	a_2	K	983.9
a_3	K	861.8	$\widetilde{k}$	-	500
γ_{mg}	N/m	$0.04582 - 0.00056 \times T$	γ_{cg}	N/m	$0.06323 - 0.00077 \times T$
γ_{mc}	N/m	0.0061	γ_{gb}	N/m	0.00061
W_{c0}	J/m^3	0.4368×10^6	W_{c1}	J/m^3	-0.0256×10^6
W_{h0}	J/m^3	0.0257×10^6	W_{h1}	J/m^3	-0.1190×10^6
W_{d0}	J/m^3	0.0001×10^6	W_{d1}	J/m^3	-0.0011×10^6
$k_{\varrho 0}$	J/m	0.0144×10^{-6}	$k_{\varrho 1}$	J/m	-0.0045×10^{-6}
k_{c0}	J/m	0.0049×10^{-6}	k_{c1}	J/m	-0.0223×10^{-6}
k_{m0}	J/m	0.0005×10^{-6}	k_{m1}	J/m	-0.0009×10^{-6}
$k_{\eta 0}$	J/m	0.00002×10^{-6}	$k_{\eta 1}$	J/m	-0.0002×10^{-6}
k_{ht}	-	3×10^{-3}			

All energy parameters W_c, W_h, W_d, k_ϱ, k_η, k_c, and k_m are solely functions of temperature and are independent of the order parameters. In this context, these parameters are considered to be

first-degree linear functions of temperature, which are expressed as:

$$W_{\mathrm{a}}(T) = W_{\mathrm{a0}} + W_{\mathrm{a1}}\tilde{T} \quad (a = \mathrm{c}, \mathrm{h}, \mathrm{d}), \tag{23}$$

$$k_{\mathrm{b}}(T) = k_{\mathrm{b0}} + k_{\mathrm{b1}}\tilde{T} \quad (b = \varrho, \mathrm{c}, \mathrm{m}, \eta), \tag{24}$$

$$\tilde{T} = (T - T_{\mathrm{m}})/T_{\mathrm{m}}, \tag{25}$$

where $\tilde{T}$ is the normalized temperature relative to the melting point T_{m}. The fitting procedures for determining parameters in Eqs. (23) and (24) are detailed in Supplementary Note 3. Given the interface width of the grain boundaries δ_{gb} to be 0.5 μm, the fitting results of the energy parameters are presented in Table 1.

The PFM governing equations in Eqs. (9), (10), (11) and (13) are solved by programing and coding in the finite element method framework via the Multiphysics Object-Oriented Simulation Environment (MOOSE) platform [54]. In the following section, we show a series of 2D simulations to explore the crystallization behavior of iPP composite under cooling conditions that are typical during 3D printing process.

4. Results and discussions

4.1. Benchmark simulation on isothermal crystallization of iPP polymer

This subsection introduces a benchmark problem for a pure iPP polymer, utilizing a 2D simulation box with dimensions of 40 μm × 40 μm (240 × 240 meshes), as illustrated in Fig. 4(a). At the start of each simulation, the polymer is assumed to be in a completely molten state, with no initial crystalline nuclei present and a initial temperature of 460.7 K. To maintain the isothermal conditions, Dirichlet boundary conditions for temperature are applied to the top and bottom boundaries ($T_1 = T_2 = T_{\mathrm{set}}$). Fig. 4(b) illustrates the temporal crystalline evolution at 340 K. The blue color represent the molten polymer state, while the other colors represents distinguish assignments of the OPs $\{\eta_i\}$ to differentiate the crystalline grains. Initially, no crystalline structure exists in the system. Over time, new nuclei form and gradually grow, eventually occupying the entire polymer domain. Then a series of simulations are conducted, with a constant temperature T_{set} ranging from 340 K to 380 K with a increment of 10 K. The ultimate polymer crystalline morphology after solidification is illustrated in Fig. 4(c). In this figure, the crystalline structures can be observed within the box, showing a noticeable decrease of nuclei number and an increase of average crystalline sizes at elevated temperatures. As the temperature cools down from the melting point, the material undergoes sporadical nucleation. After nucleation, the grains grow and eventually come into contact with one another, which limits the available space for new nuclei formation and ultimately leads to a saturation of the nuclei density. The saturated nuclei density at various temperatures is presented in Fig. 4(d) with the yellow markers, showing an inverse relationship

with the temperature. With the increase of temperature, the nucleation rate decreases to reduce the number of nuclei, finally increasing crystalline size. The results are consistent with the theoretical model in the literature [45] (represented by the blue line in Fig. 4(d)). Furthermore, the simulated crystallization half-time $t_{0.5}$, defined as the time at which the material attains half of its ultimate crystallinity, is compared with existing experimental data from [55] and [56], as shown in Fig. 4(e). Our simulation results exhibit the trends that are generally consistent with the experimental data and fall to the experimentally reported range, thus validating our proposed PFM.

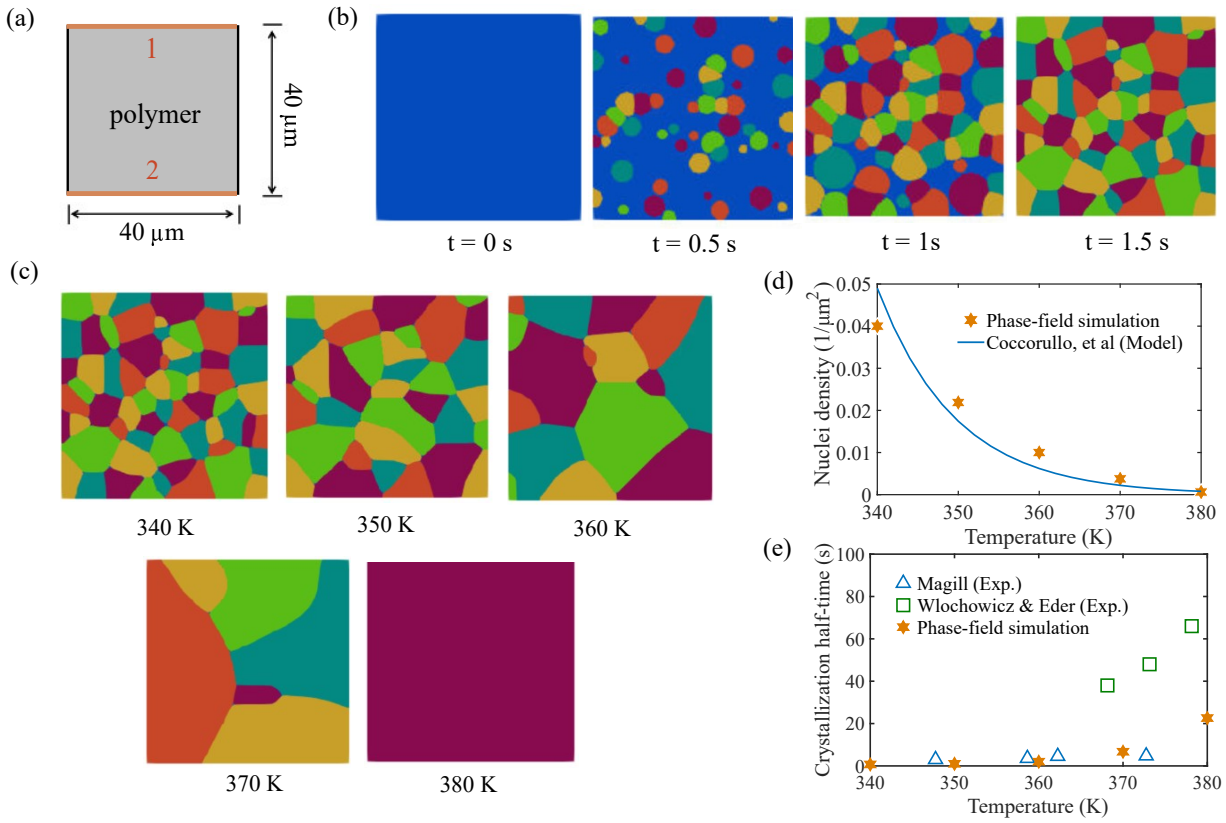

Fig. 4. (a) Schematic representation of the simulation box for isothermal polymer crystallization; (b) Temporal evolution of the crystalline morphology at 380 K, where the blue color indicates the molten polymer, and other colors represent the OPs of the crystalline grains $\{\eta_i\}$; (c) Final crystalline grain morphology within the polymer at temperatures of 340, 350, 360, 370, and 380 K; (d) Comparison of the relationship between the saturated nuclei density and temperature in our simulation with the theoretical model from [45]; (e) Comparison of the relationship between the isothermal crystallization half-time in our simulation with the experimental data from [55, 56].

4.2. Non-isothermal crystallization of iPP composite during 3D printing

We then move to our focus on crystallization morphology along the fibers within the polymer. It should be noted that we do not intend to reproduce the real printing process. Instead, this analysis

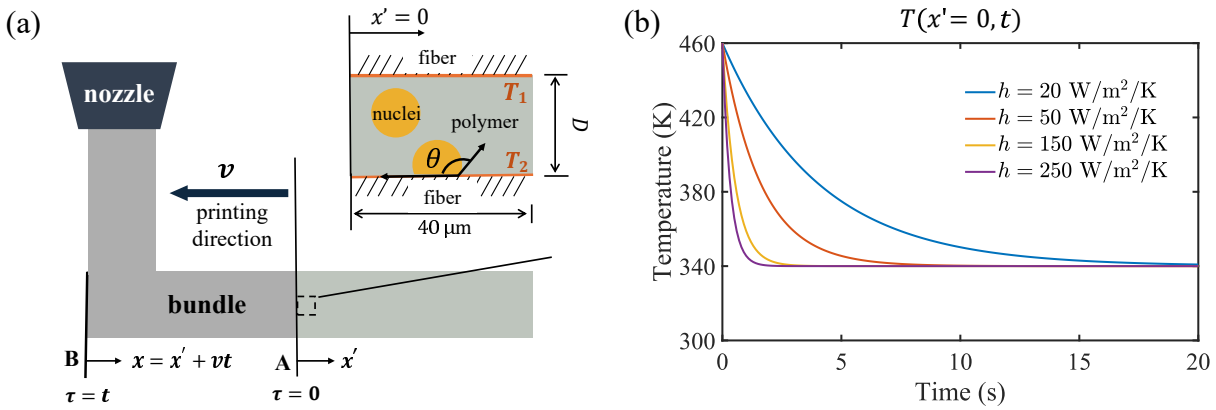

Fig. 5. (a) Schematic diagram of the model setup during the 3D printing process; (b) Temperature evolution at position **A** of the bundle ($x' = 0$) over time t.

delves into the non-isothermal crystallization behavior of iPP composites during 3D printing. A schematic representation of the model setup is provided in Fig. 5(a). At time $\tau = 0$, the bundle is deposited onto the printing bed with its front initially positioned at position **A**. With a constant printing speed v, the bundle front advances to position **B** after a time interval t. During this process, the temperature of the printing bundle decreases from an initial value of T_0 to the ambient temperature T_∞, due to interaction with the surrounding air. In the subsequent studies, we assume a uniform temperature distribution across the bundle cross-section (the plane with x direction as the normal vector), which is a reasonable approximation given the small size of the simulation domain. At time $\tau = t$, the temperature profile along the bundle length (along x length), according to the literature [57], can be analytically represented by:

$$T(x) = T_\infty + (T_0 - T_\infty)\mathrm{e}^{-x \cdot m(h)}, \tag{26}$$

where x denotes the distance along the x-axis from position **B**, h is the convective heat transfer coefficient. The parameter $m(h)$ is determined by the thermal diffusivity α and the heat transfer coefficient $\beta(h)$, which is written as $m = [\sqrt{1 + 4\alpha\beta(h)} - 1]/2\alpha$. The coefficients α and β are defined as $\alpha = k_T/(\rho C_\mathrm{p} v)$ and $\beta = h\rho C_\mathrm{p} A v/P_\mathrm{c}$, respectively, with P_c representing the perimeter and A the elliptical cross-section area of the bundle.

The simulation domain is fixed within the bundle with its front located at position **A**, as show in Fig. 5 (a). It encompasses the polymer region between two adjacent continuous fibers, with dimensions of 40 μm in length and a variable height of D μm. A Dirichlet boundary condition for the temperature is applied to the top ($T_1(x', t)$) and bottom ($T_2(x', t)$) boundaries based on the analytical expression given in Eq. (26). Here, x' denotes the distance along the x-axis from position **A**. By substituting $x = vt + x'$ into Eq. (26), we obtain

$$T_1(x', t) = T_2(x', t) = T(vt + x'). \tag{27}$$

The initial deposition temperature T_0 is set to 460 K, while the ambient temperature T_∞ is maintained at 340 K. Additionally, the bundle is assumed to have a circular cross-section of 200 μm radius, and the printing velocity is set at 10 mm/s. The temperature evolution at the leading edge of the bundle ($x' = 0$) over time t is depicted in Fig. 5(b), demonstrating that an increased convective heat transfer coefficient h leads to a more rapid cooling towards the ambient temperature.

Initially, a simulation is conducted with the conditions: a contact angle θ of 90°, a fiber spacing D of 24 μm, and a convective heat transfer coefficient $h = 150$ W/m^2/K. This simulation assumes no void/gas phase ($\varrho = 1$). The applied temperature condition, as delineated by Eq. (26), is depicted in Fig. 5(b) with $h = 150$ W/m^2/K. At the initial time $t = 0$ s, the temperature is 460 K. Then it rapidly decreases due to effective heat exchange with the surrounding air and eventually stabilizes at 340 K after 3 s of cooling. During the cooling period, the evolution of the crystalline morphology is depicted in Fig. 6(a), where the blue color indicates the molten polymer phase and the other colors in the polymer domain map to order parameters $\{\eta_i\}$ that differentiate between distinct crystalline grains. At time $t = 0$ s, the material is molten at the onset of the deposition. After a cooling period of 1 s, numerous crystalline grains can be observed on the fiber surface, whereas no grains emerge within the polymer interior, as illustrated in the snapshot at $t = 1$ s in Fig. 6(a). As time advances to $t = 2$ s, a distinctive columnar crystalline structure emerges on the fiber surface, known as the TCL, due to the constrained lateral growth of individual crystalline grains. Simultaneously, in the polymer regions away from the fiber, spherulite structures emerge and intersperse among the TCL. As the time extends from 2 s to 3 s, the crystalline grains grow until the polymer is completely filled with the crystalline phase, as illustrated in the snapshot at $t = 3$ s in Fig. 6(a). Building on the simulation in Fig. 6(a), we now incorporate the potential presence of void/gas phases with evolving ϱ. The corresponding microstructure evolution is presented in Fig. 6(b), where blue denotes the molten polymer, white indicates voids, and other colors correspond to crystalline grain OPs η_i. The simulation begins with randomly distributed voids of varying sizes and shapes. By $t = 1$ s, the voids become more circular due to the surface tension effect. Meanwhile, the void shrinks due to diffusion-induced dissolution of the voids into the resin [58]. As temperature further decreases, void mobility decreases. Thus, it can be seen in the snapshot at $t = 3$ s that larger voids become trapped between growing crystalline domains while smaller voids completely dissolve. Additionally, compared with Fig. 6(a), the presence of voids shows no significant effect on the crystalline morphology evolution. Since our primary focus here is crystalline development, we will disregard voids in the subsequent analyses and simulations; nevertheless, the void evolution is pivotal to final part quality and will therefore be investigated comprehensively in our future work.

The crystallization mechanism for the gas-free case (Fig. 6(a)) is further analyzed in Fig. 7. To examine the nucleation events during polymer crystallization, the temporal variation of nuclei

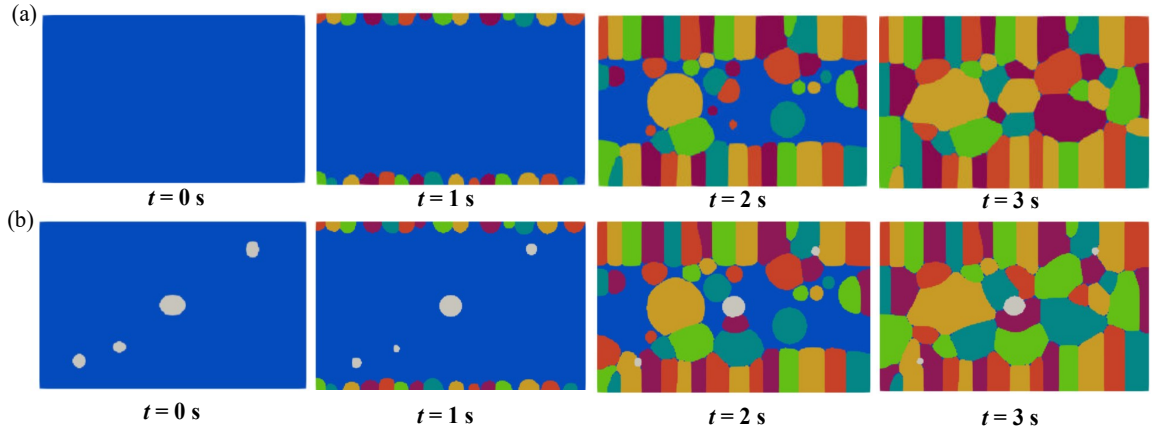

Fig. 6. Morphological evolution of the crystalline structure at various time (a) without void ($\varrho = 1$) and (b) with void (ϱ evolution). The blue color indicates the molten polymer, white denotes the void, and the other colors represent the OPs of crystalline grains $\{\eta_i\}$. In both two scenarios, the parameters are set as $\theta = 90°$, $D = 24$ μm, and $h = 150$ W/m^2/K

counts is plotted in Fig. 7(a). The solid line (N_{hetero}) indicates the nuclei count on the fiber surface, in corresponding to the heterogeneous nucleation process (as described in Fig. 3(a)). The dashed line (N_{homo}) represents the nuclei count within the polymer interior, in corresponding to the homogeneous nucleation process. It is observed that N_{hetero} exhibits an earlier onset and a more rapid rate of increase as compared to N_{homo}, owing to the enhanced nucleation rate on the fiber surface. After nucleation, these newly formed nuclei further evolve into crystalline grains, competing for spatial availability. To evaluate the impact of fiber on the crystalline growth, the average crystalline grain areas are calculated, considering two scenarios distinguished by their nucleation origins: heterogeneous and homogeneous nucleation, as presented in Fig. 7(b). These average crystalline areas are calculated using the respective formulas $A_{\text{hetero}} = S_{\text{hetero}}/N_{\text{hetero}}$ for the heterogeneous group (solid line) and $A_{\text{homo}} = S_{\text{homo}}/N_{\text{homo}}$ for the homogeneous group (dashed line), where S_{hetero} and S_{homo} denote the total crystalline areas associated with each group. It can be observed that the slopes of the solid and dashed lines in Fig. 7(b) are similar. Nevertheless, the structural morphologies of these two scenarios are different (Fig. 6(a)): the transcrystalline (solid line) grows as parallel columns, whereas the spherulite (dashed line) develops in a radial, sphere-like fashion. This implies that the distinct morphologies between TCL and spherulitic structures have minimal influence on the average rate of crystalline growth. Furthermore, to examine the crystallization kinetics, the relative crystallinity R is plotted against time in Fig. 7(c). This parameter represents the ratio of the current crystallinity to the ultimate crystallinity within the material. It is obtained from the average value of ϕ_c throughout the simulation domain. As shown in Fig. 7(c), the relative crystallinity experiences an accelerated rate of increase and then gradually slows

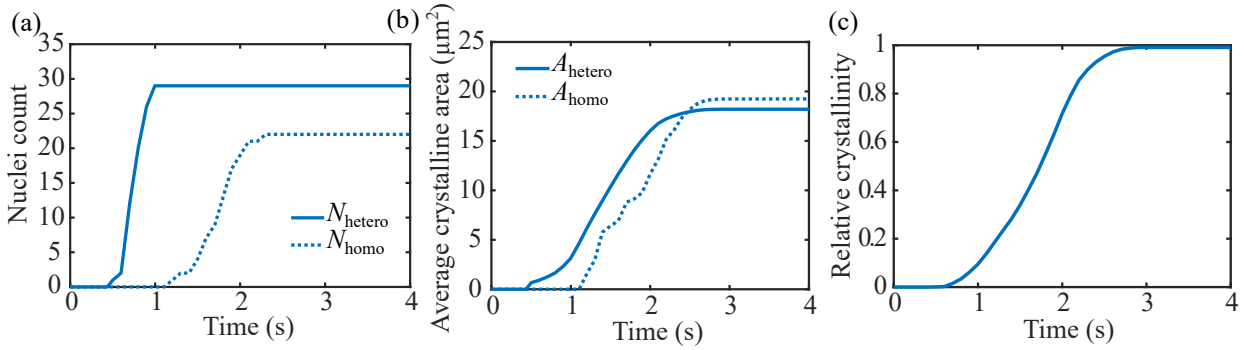

Fig. 7. For the scenario without gas (Fig. 6(a)): (a) Evolution of nuclei count over time for heterogeneous nucleation (N_{hetero}) and homogeneous nucleation (N_{homo}) ; (b) Evolution of average area occupied by crystalline grains, categorized based on: heterogeneous nucleation (A_{hetero}) and homogeneous nucleation (A_{homo}); (c) Relative crystallinity R evolution over time.

down, eventually approaching the saturated value of 1 which indicates the completeness of crystallization. The commencement of the crystallinity development is consistent with the onset time in N_{hetero}. Thus, it is governed by the initial nucleation events occurring on the fiber surface. The subsequent increase rate in R is related to both the nuclei count and crystalline growth rate, which collectively determine the crystallization time.

During the crystallization process, numerous factors, such as the convective heat transfer coefficient h, contact angle θ, and fiber spacing D, can significantly affect the nucleation and crystalline growth behavior of the crystalline material, which further determines the material morphology and the crystallization kinetics. To elucidate the effect of these parameters on the TCL growth mechanism, a series of simulations have been conducted.

4.3. Effect of the contact angle

The influence of contact angle θ in the crystallization behavior of iPP composites is examined for θ at 90°, 100°, 112°, and 180°, as illustrated in Fig. 8. During the simulation, the fiber spacing is maintained at 24 μm, and the convective heat transfer coefficient is fixed at $h = 150$ W/m^2/K. The ultimate morphology of crystalline grains is shown in Fig. 8(a). It shows that at a low θ values of 90° and 100°, the fiber surface displays a distinct columnar structure, known as TCL. However, as θ increases to 180°, the TCL structure disappears. This is due to the reduction in nuclei count on the fiber surface as θ increases, since a high density of nuclei is necessary to facilitate the TCL formation. The temporal evolution of the nuclei count is then examined, with N_{hetero} designating heterogeneous nucleation on the fiber surface (Fig. 8(b)) and N_{homo} representing homogeneous nucleation within the polymer interior (Fig. 8(c)). For N_{hetero}, as θ decreases, nucleation events occur at an earlier stage, and the nuclei count accumulates at a faster rate. This results in a higher

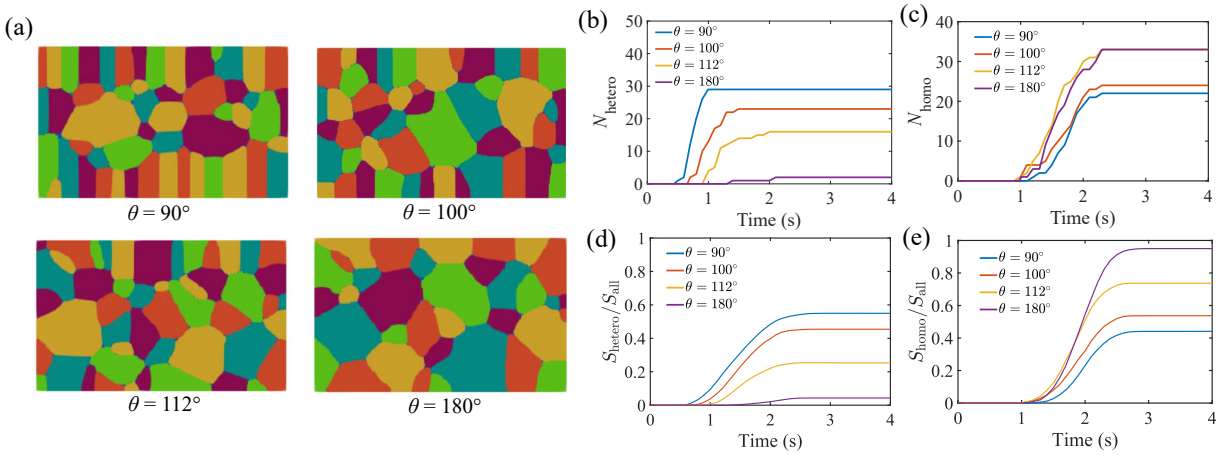

Fig. 8. Effects of the contact angle θ on the crystallization behavior of iPP composites with θ = 90°, 100°, 112°, and 180°, and with fixed D = 24 μm and h = 150 W/m^2/K: (a) Morphological evolution of crystalline structure; Temporal evolution of (b) the heterogeneous nuclei count N_{hetero}, (c) the homogeneous nuclei count N_{homo}, (d) the crystalline area ratio $S_{\text{hetero}}/S_{\text{all}}$, and (e) the crystalline area ratio $S_{\text{homo}}/S_{\text{all}}$.

saturated nuclei count within a shorter period, thereby facilitating TCL formation. This trend is attributed to the enhanced nucleation rate on the fiber surface at lower θ. In contrast, N_{homo} in Fig. 8(c) exhibits a similar induction period for nucleation events across varying contact angles. However, at higher contact angles (112° and 180°), N_{homo} demonstrates both a faster growth rate and a greater saturation value comparing to those at lower contact angles (90° and 100°). This is because the diminution of the TCL structure at higher contact angles permits a larger space for homogeneous nucleation events to occur within the polymer. This indicates a competition between TCL and spherulites for space occupancy. To further elaborate on this spatial competition, the growth of the crystalline areas within the polymer matrix is illustrated in Fig. 8(d) and (e), considering two distinct nucleation mechanisms. The crystalline area ratio from heterogeneous nucleation ($S_{\text{hetero}}/S_{\text{all}}$) is shown in Fig. 8(d), while the crystalline area ratio from homogeneous nucleation ($S_{\text{homo}}/S_{\text{all}}$) is shown in Fig. 8(e). Here, S_{hetero} and S_{homo} denote the total crystalline areas originating from heterogeneous nuclei and homogeneous nuclei, respectively. S_{all} represents the total area of the polymer domain. It is found that a lower contact angle leads to a greater $S_{\text{hetero}}/S_{\text{all}}$, indicating the presence of a thicker TCL (if it exists) on the fiber surface. Conversely, the saturated value of $S_{\text{homo}}/S_{\text{all}}$ (Fig. 8(e)) increases with the contact angle. Thus, $S_{\text{homo}}/S_{\text{all}}$ and $S_{\text{hetero}}/S_{\text{all}}$ exhibit an inverse relationship with the contact angle. This is due to the spatial competition between heterogeneous and homogeneous nucleation domains, where the total crystallization area is fixed. This competition is primarily governed by the nucleation events. The increase in nuclei density on the fiber surface at lower θ enhances the competitiveness of these surface nuclei relative to the interior nuclei for spatial dominance, thereby promoting the formation of a thicker

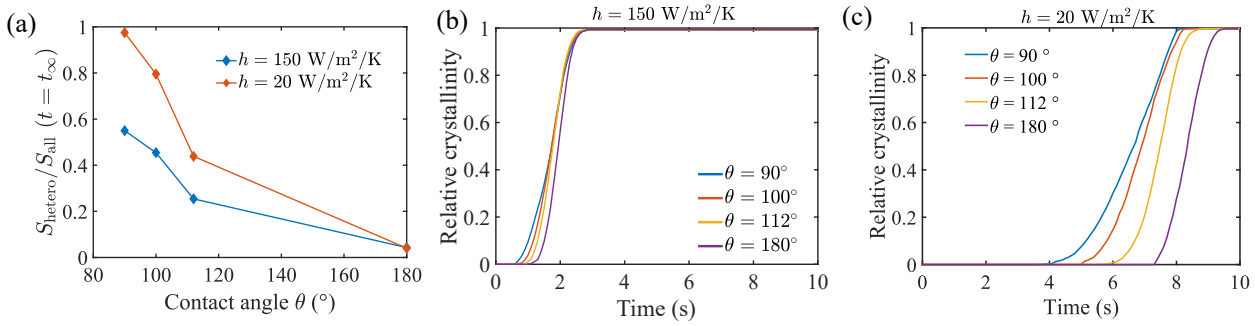

Fig. 9. (a) Comparison of correlation between crystalline area ratio $S_{\text{hetero}}/S_{\text{all}}$ and contact angle θ at h = 150 W/m^2/K and h = 20 W/m^2/K; Relative crystallinity evolution over time for (b) varying θ at h = 150 W/m^2/K and (c) varying θ at h = 20 W/m^2/K.

TCL. Similar observations are reported in numerous experiment studies [16, 17], in which the impact of varying surface energy or varying heterogeneous nucleation capability on the TCL growth is investigated and the TCL thickness could significantly affect the mechanical properties and fracture behavior of composite materials. We remark that our previous results covered the case where the convective heat transfer coefficient is set to h = 150 W/m^2/K. Additionally, we also explored the impact of θ under conditions of a reduced cooling rate with h = 20 W/m^2/K. The related results are provided in Fig. S1 of the Supplementary Material.

The comparison of θ effect on the composite crystallization process under different cooling conditions is illustrated in Fig. 9. The ultimate ratio $S_{\text{hetero}}/S_{\text{all}}$ at the equilibrium time $t = t_\infty$ is presented in Fig. 8(a). The figure shows that the ratio $S_{\text{hetero}}/S_{\text{all}}$ for both h = 150 (blue line) and h = 20 W/m^2/K (orange line) decreases monotonically with increasing contact angle and attains a similar minimal value at θ = 180°, where no TCL is formed. Nevertheless, the ratio $S_{\text{hetero}}/S_{\text{all}}$ with a lower h (orange line) remains higher in comparison to that with a larger h (blue line) at equivalent contact angles, resulting in a steeper slope in the correlation between $S_{\text{hetero}}/S_{\text{all}}$ and θ. This observation implies that a reduced h, indicative of a slower cooling process, amplifies the effect of lower contact angle in facilitating the formation of a thicker TCL. Furthermore, the crystallinity evolution over time for varying contact angles is compared for h = 150 (Fig. 9(b)) and 20 W/m^2/K (Fig. 9(c)). The two figures demonstrate that the contact angle increase prolongs the crystallization onset period, yet enhances the crystallinity growth rate due to the faster expansion of spherulitic structures. The total crystallization time depends both on the crystallization onset period and the crystallinity growth rate. Under the rapid cooling condition (h = 150 W/m^2/K), although the rise of θ leads to a prolongation in the crystallization onset, it is insignificant and is followed by a more expedited crystallization process. As a result, the total crystallization time among varying θ shows a comparable value. Conversely, under the slow cooling condition (h = 20

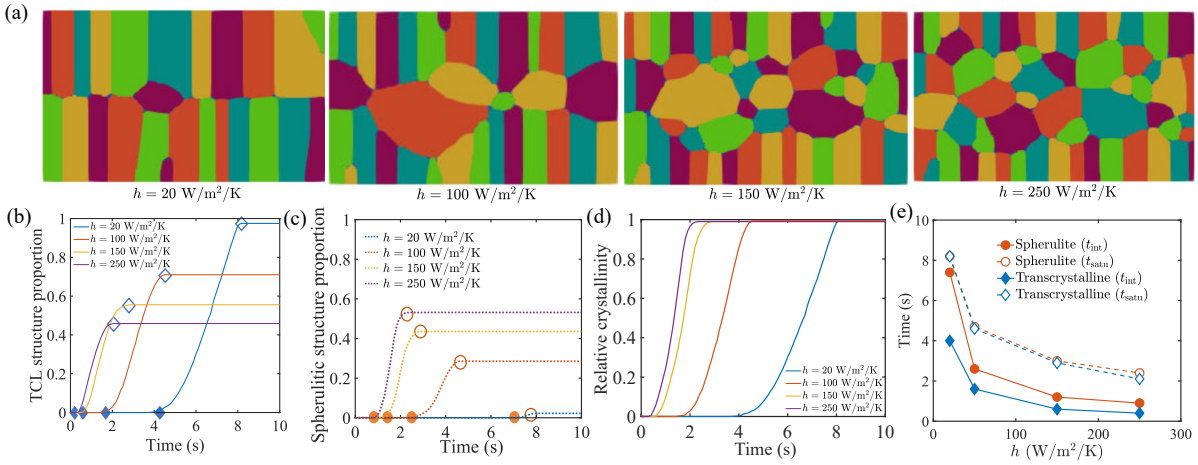

Fig. 10. Impact of convective heat transfer coefficient h on crystallization behavior of iPP composites with h = 20, 50, 150, and 250 W/m^2/K, and with fixed $\theta = 90°$ and D = 24 μm: (a) Morphological evolution of crystalline structure; (b) Ratio of TCL area over time. The blue solid rhombus symbols indicate the initial time t_{int} for ratio increase, whereas the blue open rhombus symbols indicate the saturated time t_{satu} for the ratio to stop increasing; (c) Ratio of spherulitic structure area over time. The orange solid circular symbols indicate the initial time t_{int}, whereas the orange open circular symbols indicate the saturated time t_{satu}; (d) Evolution of crystallinity over time; (e) t_{int} and t_{satu} in TCL and spherulic structure for as a function of h.

W/m^2/K), the variation in the onset time for different θ is more pronounced and cannot be offset by the faster growth in crystallinity, leading to a longer crystallization time for the increased θ. Thus, the slower cooling condition highlights the effect of lower contact angles on the enhancement of TCL fraction and the reduction in crystallization time.

4.4. Influence of the cooling condition

To delineate the underlying mechanism through which the cooling conditions affect the polymer crystallization behavior, a comparative analysis of various convective heat transfer coefficients h has been conducted, as illustrated in Fig. 10. The contact angle is set at 90° to faciliate the TCL formation. The analysis includes a series of h ranging from 20 to 250 W/m^2/K. The associated temperature profiles are presented in Fig. 5(b), which demonstrates a steeper temperature decline with the rise in h. Fig. 10(a) presents the final crystalline morphology across varying thermal conditions, revealing that a higher h promotes the spherulitic structure development while reducing the TCL proportion. Furthermore, the temporal changes in the proportion of the TCL and spherulitic structures are depicted in Fig. 10(b) and (c), respectively. These proportions are calculated using the expressions $S_{\text{hetero}}/S_{\text{all}}$ and $S_{\text{homo}}/S_{\text{all}}$, as the same as in Fig. 8(d) and (e). The solid symbols in both figures represent the initial time required for the onset of proportion growth (t_{int}), while the open symbols denote the time at which the proportion attains its saturated value and stops increasing (t_{satu}). The figures reveal that for both the TCL (blue rhombus symbols) and

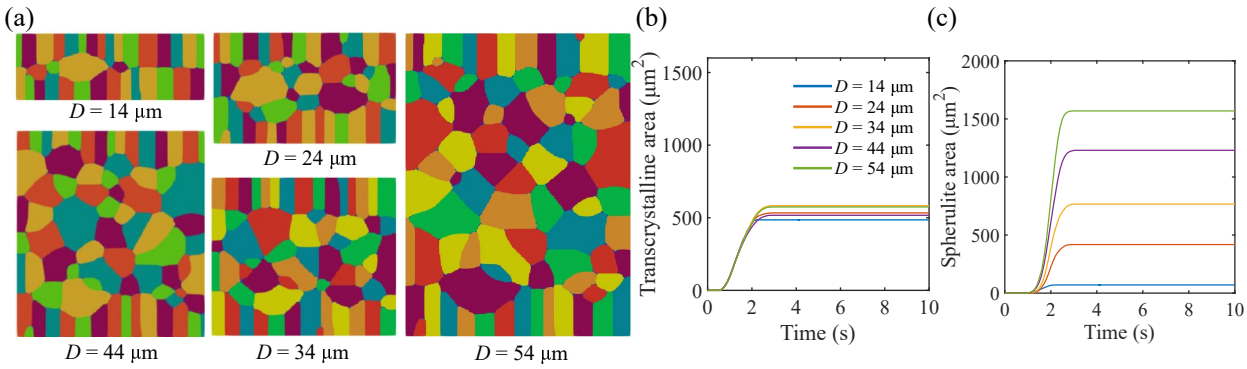

Fig. 11. Impact of fiber spacing D on the crystallization behavior of iPP composites examined at distances ranging from 14 μm to 54 μm, with fixed parameters $\theta = 90°$ and $h = 150$ W/m^2/K: (a) Morphological evolution of the crystalline structure; (b) Evolution of TCL area over time; (c) Evolution of spherulitic area over time. Panels (b) and (c) share the same legend.

the spherulitic structure (orange circular symbols), a decrease in h results in a pronounced retardation of t_{int}, along with a decline in the increasing rate of the proportion. These phenomena can be attributed to the gradual decline in temperature at lower h values, which mitigates the enhancement of nucleation rates and crystalline growth rates. This ultimately contributes to an extended polymer crystallization time, as depicted in Fig. 10(d). Moreover, the final TCL proportion at $t = t_{\text{satu}}$ decreases as h rises, whereas the final fraction of spherulitic structure exhibits an inverse relationship with h. To elucidate this discrepancy, the initial times t_{int} and the saturation times t_{satu} for the TCL and spherulitic structure are presented in Fig. 10(e). The figure shows that both the times t_{int} and t_{satu} diminish with increasing h, suggesting an acceleration in crystallization process under a more rapid cooling condition. Additionally, t_{satu} for both the TCL and spherulitic structure across varying h are close to each other (open symbols), indicating a nearly uniform crystallization time for these two structures. However, t_{int} of the spherulitic structure remains greater than that of the TCL (solid symbols), which narrows the time proportion ($\frac{t_{\text{satu}}-t_{\text{int}}}{t_{\text{satu}}}$) available for the spherulite to develop compared to the TCL. This discrepancy becomes more pronounced as h decreases, as the TCL has a longer time to develop and covers a larger area prior to the initiation of spherulitic growth, thereby leading to an increased fraction of the TCL. In other words, the condition of slow cooling amplifies the ability of the fiber surface to reduce the crystallization onset time, thereby enhancing the spatial occupancy preference of TCL over the spherulitic structure.

4.5. Influence of the fiber spacing

In addition to the contact angle and the cooling condition, the distance between adjacent fibers also influences the crystallization behavior, which is associated with factors such as pressure, fiber volume fraction, and fiber diameter. A series of fiber spacings D ranging from 14 to 54 μm

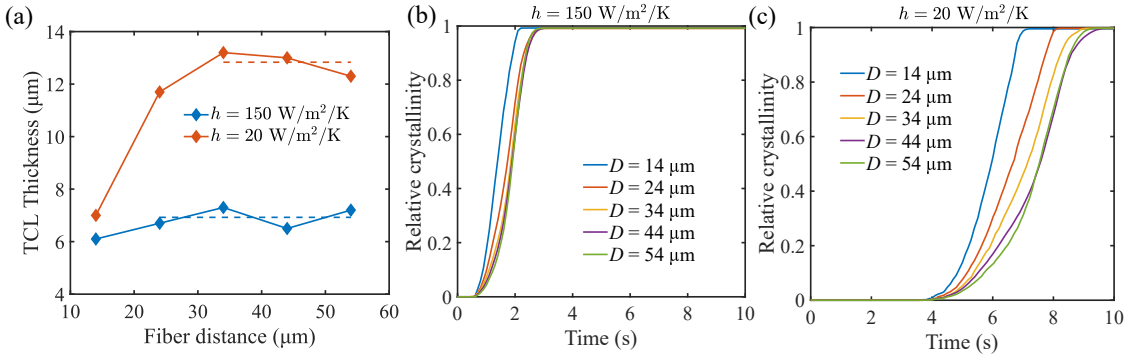

Fig. 12. (a) Comparison of the correlation between the ultimate TCL thickness and fiber distance D at $h = 150$ and 20 W/m^2/K; Relative crystallinity evolution over time for varying D at (b) $h = 150$ and (c) 20 W/m^2/K.

have been examined, with $\theta = 90°$ and $h = 150$ W/m^2/K. The resulting crystalline morphologies are presented in Fig. 11(a). At a distance of 14 μm, only a minor of spherulites is observed between the intersecting TCL. With an increase in fiber spacing, the occupied area of spherulites significantly increases, whereas the TCL area exhibits relatively minimal variation. The temporal evolution of TCL areas (S_{hetero}) and spherulite areas (S_{homo}) are plotted in Fig. 11(b) and Fig. 11(c), respectively. It can be seen that the TCL development is only marginally affected by fiber spacing (Fig. 11(b)). In contrast, the expansion rate of spherulitic structure considerably increases with greater inter-fiber spacings, due to the expanded space allowing for more nucleation events to occur within the polymer interior (Fig. 11(c)). Moreover, the impact of fiber spacing is further investigated under a slow cooling condition of $h = 20$ W/m^2/K, as depicted in Fig. S2.

The impacts of fiber spacings on crystallization behavior are compared for different thermal conditions, as illustrated in Fig. 12. The relationship between TCL thickness and fiber spacings is explored across varying h (Fig. 12(a)). The TCL thickness is calculated by $\frac{S_{\text{hetero}}}{2L}$, where L refers to the simulation box length. The factor of 2 in the denominator accounts for the presence of two fiber surfaces at the top and bottom boundaries. It shows that, for both cooling conditions, as D increases from 14 to 54 μm, the TCL thickness initially increases, then levels off and varies around an average value (represented by the dashed lines). This is because at narrower fiber spacings, the TCL growth is spatially constrained, leading to the contact of adjacent TCLs, leaving minimal space for spherulite formation between the TCLs. As D increases, the TCL gains more space to grow and increases the thickness. However, this TCL growth is counterbalanced by the concurrent expansion of spherulitic structures, ultimately reaching a saturation point in thickness. At this point, the boundaries of TCL intersect with those of the spherulites. Further increments in D lead to fluctuations rather than consistent increases in TCL thickness. The saturated thickness of the TCL exhibits variations under different conditions. Under slower cooling conditions, such as $h = 20$ W/m^2/K, the TCL develops more extensively, resulting in a greater saturated thickness at

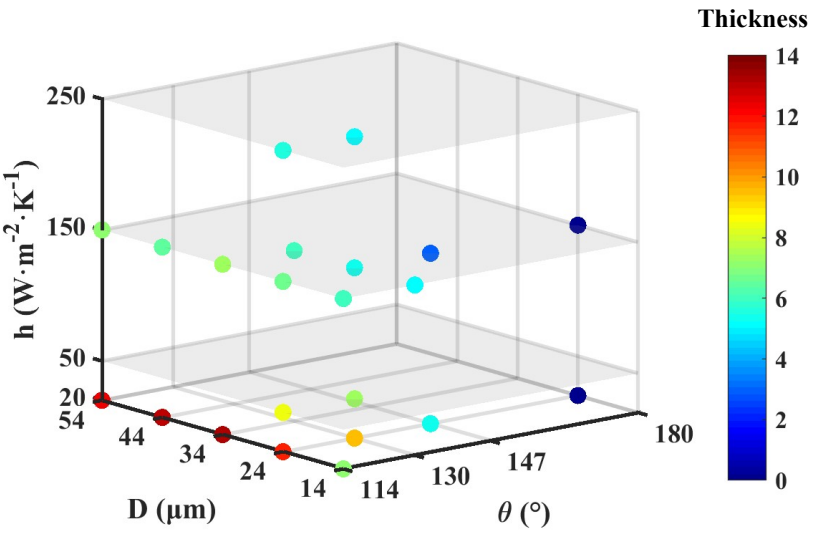

Fig. 13. Scatter plot of simulated TCL thickness under varying contact angle θ, fiber spacing D, and the convective thermal coefficient h

a higher D compared to the faster cooling condition of h = 150 W/m^2/K. Furthermore, the impact of fiber spacing on the crystallinity evolution is examined for h = 20 (Fig. 12(b)) and 150 W/m^2/K (Fig. 12(c)). It is observed from Fig. 12(b) that the crystallization time increases with higher D and stabilizes when D exceeds 24 μm. Similarly, in Fig. 12(c), the crystallization time increases with rising D and then stabilizes when D exceeds 44 μm. This is because when TCL predominates in polymer crystallization, the larger fiber spacing extends the time for TCL to fully develop in the thickness direction, thereby extending the overall crystallization time. Conversely, when spherulites dominate the crystallization process, the nuclei density and the crystalline growth rate show minimal variation across different spatial areas, leading to a close duration for crystallization to be completed. The predominance of TCL within the polymer matrix can be directly attributed to the significantly larger proportion of TCL comparing to spherulites. This disparity between the TCL and spherulitic area is accentuated under the condition of the slower cooling. Consequently, under these conditions, a larger critical fiber spacing D is required to ensure the dominance of spherulites, thereby achieving stabilization in the crystallization time. Thus, an increase in fiber spacing promotes the TCL growth, leading to thicker TCL and extended crystallization periods. However, the TCL expansion is ultimately limited by the spherulites development, which eventually saturates the TCL thickness and crystallization time.

4.6. Discussion

Fig. 13 summarizes the simulated TCL thickness for varing contact angle θ, fiber spacing D, and convective heat-transfer coefficient h. Red denotes the thickest TCL, blue the thinnest. The thickest TCLs (red) concentrate where h and θ are low and D is high, defining a process window that promotes TCL growth. Conversely, the thinnest TCLs (blue) appear where h and θ are high and D is low. These findings offer quantitative guidelines for selecting process parameters to either maximize or minimize TCL thickness in future experiments. Furthermore, our results could also provide insights into some of the conflicting findings in experiments regarding the TCL growth mechanism. For example, Moon et al. [23] observed that the thickness of the TCL decreases with increasing fiber diameter. However, Pompe et al. [22] found no correlation between TCL thickness and fiber diameter. In these two studies, the fiber spacing significantly exceeds the TCL thickness, and no intersecting TCL boundaries are observed. As indicated by our simulation results (Fig. 11 and Fig. 12(a)), within the range of fiber spacing in the studies [23] and [22], the TCL thickness reaches a saturation limit as fiber spacing increases. Thus, in these two studies, the effect of fiber spacing is negligible. However, the characteristics of the fiber surface, related to the fiber diameter, can influence its nucleation abilities, further affecting the TCL thickness. In the work of Moon et al. [23], the TCL thickness decrease with larger fiber diameter may be explained by the increase of wetting force on the fiber surface. This could enhance the nucleation ability on the fiber surface with a smaller contact angle θ. Thus, this would further increase the TCL thickness, which is consistent with our observations in Fig. 8. In contrast, in the work of Pompe et al. [22], the specific chemical treatments of the fiber surface could leave the contact angle θ insensitive to fiber diameter variation. In this way, the TCL thickness remains unchanged with fiber diameter variation. Thus, the variation of fiber interface characteristics (or contact angle θ) would primarily determine the TCL thickness, which could explain the conflict results observed in [23] and [22].

5. Conclusion

To conclude, a non-isothermal phase-field model is developed to mesoscopically simulate the crystallization morphology evolution of CFRTPCs during 3D printing. The PFM is derived from a free energy density functional incorporating order parameters to describe crystallization, with phase-field evolution equations intrinsically coupled to heat transfer. Particularly, the fiber-crystalline-melt contact angle dependent sporadic nucleation processes are integrated into the PFM and are numerically implemented by using an explicit nucleation algorithm. The model is capable of capturing key microstructural evolution phenomena during thermoplastic crystallization, including crystalline growth and void dissolution. A special focus is placed on the TCL evolution mechanism, examining the impacts of fiber surface characteristics, spacing, and cooling

conditions. Simulation results reveal that the TCL thickness can be augmented by decreasing the contact angle and slowing the cooling rates. Additionally, an increase in fiber spacing permits the TCL thickness to increase until reaching a stable region. The effects of contact angle and fiber spacing on the TCL thickness can be amplified under the slow cooling condition. These behaviors stems from the competition between TCL and spherulites for spatial occupation.

The proposed PFM provides an effective computational framework for simulating mesoscopic microstructure evolution in thermoplastic composites during 3D printing. Future work will extend the model to incorporate the mechanical effects during solidification. This research is expected to lay the groundwork for optimizing the manufacturing processes of thermoplastic composites from a mesoscopic point of view, potentially enhancing their material properties and performance in practical applications.

Acknowledgement

The authors acknowledge the support from the National Natural Science Foundation of China (NSFC, 12372106), the Fundamental Research Funds for the Central Universities, the Key Fund Projects of China Academy of Railway Sciences (2022YJ320), the Innovation Research Foundaton of COMAC-BUAA Aircraft Research Institute (24010209), the Outstanding Youth Fund of Jiangsu Province (BK20240077), the Fundamental Research Funds for the Central Universities (NE2024001), and a project Funded by the Priority Academic Program Development of Jiangsu Higher Education Institutions. This work is partially supported by High Performance Computing Platform of Nanjing University of Aeronautics and Astronautics, and High Performance Computing Platform of Beihang University.

Declaration of generative AI and AI-assisted technologies in the writing process

During the preparation of this work, the authors used ChatGPT 3.5 in order to enhance the readability of the paper. After using this tool, the authors reviewed and edited the content as needed and took full responsibility for the content of the publication.

References

[1] R. Hsissou, R. Seghiri, Z. Benzekri, M. Hilali, M. Rafik, A. Elharfi, Polymer composite materials: A comprehensive review, Composite Structures 262 (2021) 113640. doi:10.1016/j.compstruct.2021.113640.

[2] M. Barile, L. Lecce, M. Iannone, S. Pappadà, P. Roberti, Thermoplastic Composites for Aerospace Applications, Springer International Publishing, Cham, 2020, pp. 87–114. doi:10.1007/978-3-030-35346-9_4.

[3] S. Wang, X. Yan, B. Chang, J. Zhang, S. Liu, F. Liu, J. Shang, L.-H. Shao, S. Yin, W. Zhang, Y. Zhu, X. Ding, A review on modeling strategies in understanding the process mechanism of 3d printed continuous fiber-reinforced

thermoplastic composites, Journal of Manufacturing Processes 145 (2025) 46–70. doi:10.1016/j.jmapro.2025.04.014.

[4] S. Pervaiz, T. A. Qureshi, G. Kashwani, S. Kannan, 3d printing of fiber-reinforced plastic composites using fused deposition modeling: A status review, Materials 14 (2021) 4520. doi:10.3390/ma14164520.

[5] L. G. Blok, M. L. Longana, H. Yu, B. K. Woods, An investigation into 3d printing of fibre reinforced thermoplastic composites, Additive Manufacturing 22 (2018) 176–186. doi:10.1016/j.addma.2018.04.039.

[6] A. E. Moumen, M. Tarfaoui, K. Lafdi, Additive manufacturing of polymer composites: Processing and modeling approaches, Composites Part B: Engineering 171 (2019) 166–182. doi:10.1016/j.compositesb.2019.04.029.

[7] P. K. Penumakala, J. Santo, A. Thomas, A critical review on the fused deposition modeling of thermoplastic polymer composites, Composites Part B: Engineering 201 (2020) 108336. doi:10.1016/j.compositesb.2020.108336.

[8] L. Adam, O. Lietaer, S. Mathieu, I. Doghri, Numerical simulation of additive manufacturing of polymers and polymer-based composites, in: K. Friedrich, R. Walter, C. Soutis, S. G. Advani, I. H. B. Fiedler (Eds.), Structure and Properties of Additive Manufactured Polymer Components, Woodhead Publishing Series in Composites Science and Engineering, Woodhead Publishing, 2020, pp. 115–146. doi:10.1016/B978-0-12-819535-2.00005-3.

[9] M. Zhang, X. Tian, D. Li, Interfacial transcrystallization and mechanical performance of 3d-printed fully recyclable continuous fiber self-reinforced composites, Polymers 13 (2021) 3176. doi:10.3390/polym13183176.

[10] N. Ning, S. Fu, W. Zhang, F. Chen, K. Wang, H. Deng, Q. Zhang, Q. Fu, Realizing the enhancement of interfacial interaction in semicrystalline polymer/filler composites via interfacial crystallization, Progress in Polymer Science 37 (2012) 1425–1455. doi:10.1016/j.progpolymsci.2011.12.005.

[11] H. Quan, Z. M. Li, M. B. Yang, R. Huang, On transcrystallinity in semi-crystalline polymer composites, Composites Science and Technology 65 (2005) 999–1021. doi:10.1016/j.compscitech.2004.11.015.

[12] K. A. Allen, L. T. Kearney, S. Gupta, H. Ghossein, J. K. Keum, J. T. Damron, H. E. Humphrey, U. Vaidya, A. K. Naskar, Understanding interfacial crystallization dynamics on carbon fiber reinforced polypropylene composite manufacturing, Composites Part B: Engineering 291 (2025) 112027. doi:10.1016/j.compositesb.2024.112027.

[13] C. M. Wu, M. Chen, J. Karger-Kocsis, Effect of micromorphologic features on the interfacial strength of ipp/kevlar fiber microcomposites, Polymer 42 (2001) 199–208. doi:10.1016/S0032-3861(00)00312-8.

[14] J. M. Park, D. S. Kim, The influence of crystallinity on interfacial properties of carbon and sic two-fiber/polyetheretherketone (peek) composites, Polymer Composites 21 (2000) 789–797. doi:10.1002/pc.10233.

[15] J. Fang, L. Zhang, C. Li, Largely enhanced transcrystalline formation and properties of polypropylene on the surface of glass fiber as induced by pei-cnt and pei-go modification, Polymer 186 (2020) 122025. doi:10.1016/j.polymer.2019.122025.

[16] K. Cho, D. Kim, S. Yoon, Effect of substrate surface energy on transcrystalline growth and its effect on interfacial adhesion of semicrystalline polymers, Macromolecules 36 (20) (2003) 7652–7660. doi:10.1021/ma034597p.

[17] T. Hata, K. Ohsaka, T. Yamada, K. Nakamae, N. Shibata, T. Matsumoto, Transcrystalline region of polypropylene: Its formation, structure and mechanical properties, The Journal of Adhesion 45 (1994) 125–135. doi:10.1080/00218469408026633.

[18] H. Nuriel, N. Klein, G. Marom, The effect of the transcrystalline layer on the mechanical properties of composite materials in the fibre direction, Composites Science and Technology 59 (11) (1999) 1685–1690. doi:10.1016/

S0266-3538(99)00026-3.

[19] T. Ramanathan, E. Schulz, K. Subramanian, Determination of micro-hardness and elastic modulus in the transcrystalline zone of carbon fibre/pps composites using a knife edge indentor, Composites Science and Technology 65 (1) (2005) 1–7. doi:10.1016/j.compscitech.2004.04.007.

[20] H. Pérez-Martín, P. Mackenzie, A. Baidak, C. M. Brádaigh, D. Ray, Crystallinity studies of pekk and carbon fibre/pekk composites: A review, Composites Part B: Engineering 223 (2021) 109127. doi:10.1016/j.compositesb.2021.109127.

[21] C. Tung, P. Dynes, Morphological characterization of polyetheretherketone–carbon fiber composites, Journal of Applied Polymer Science 33 (2) (1987) 505–520. doi:10.1002/app.1987.070330218C.

[22] G. Pompe, E. Mäder, Experimental detection of a transcrystalline interphase in glass-fibre/polypropylene composites, Composites Science and Technology 60 (11) (2000) 2159–2167. doi:10.1016/S0266-3538(00)00120-2.

[23] C.-k. Moon, Effect of molecular weight and fiber diameter on the interfacial behavior in glass fiber/pp composites, Journal of Applied Polymer Science 67 (7) (1998) 1191–1197. doi:10.1002/(SICI)1097-4628(19980214)67:7<1191::AID-APP4>3.0.CO;2-B.

[24] N. Bigot, M. Boutaous, S. Xin, N. Hamila, Modeling heat transfer and transcrystallization kinetics during processing of polymer-based composites materials, Polymers for Advanced Technologies 34 (2) (2023) 655–675. doi:10.1002/pat.5918.

[25] A. Durin, N. Boyard, J.-L. Bailleul, N. Billon, J.-L. Chenot, J.-M. Haudin, Semianalytical models to predict the crystallization kinetics of thermoplastic fibrous composites, Journal of Applied Polymer Science 134 (8) (2017) 44508. doi:10.1002/app.44508.

[26] X. Guan, R. Pitchumani, Modeling of spherulitic crystallization in thermoplastic tow-placement process: Spherulitic microstructure evolution, Composites Science and Technology 64 (2004) 1363–1374. doi:10.1016/j.compscitech.2003.10.023.

[27] C. Ruan, J. Ouyang, S. Liu, Multi-scale modeling and simulation of crystallization during cooling in short fiber reinforced composites, International Journal of Heat and Mass Transfer 55 (2012) 1911–1921. doi:10.1016/j.ijheatmasstransfer.2011.11.046.

[28] A. Durin, J. L. Chenot, J. M. Haudin, N. Boyard, J. L. Bailleul, Simulating polymer crystallization in thin films: Numerical and analytical methods, European Polymer Journal 73 (2015) 1–16. doi:10.1016/j.eurpolymj.2015.10.001.

[29] L. Chen, Phase-field models for microstructure evolution, Annual Review of Materials Science 32 (2002) 113–140. doi:10.1146/annurev.matsci.32.112001.132041.

[30] F. Wang, W. Chen, D. Wang, H. Hou, Y. Zhao, Phase-field modeling and experimental investigation for rapid solidification in wire and arc additive manufacturing, Journal of Materials Research and Technology 28 (2024) 4585–4599. doi:10.1016/j.jmrt.2024.01.021.

[31] C. Liang, M. Xue, M. Yi, Non-isothermal phase-field modeling and simulation of microstructure evolution in magnetic field-assisted selective laser sintering, Computer Methods in Applied Mechanics and Engineering 432 (2024) 117387. doi:https://doi.org/10.1016/j.cma.2024.117387.
URL https://www.sciencedirect.com/science/article/pii/S004578252400642X

[32] K. Chang, C. Liang, M. Yi, Numerical simulation of selective laser melting by combining discrete element method and phase-field method, Chinese Journal of Computational Mechanics 41 (5) (2024) 830–836. doi:10.7511/jslx20231123003.

[33] W. Tang, Z. Tang, W. Lu, S. Wang, M. Yi, Modeling and prediction of fatigue properties of additively man-

ufactured metals, Acta Mechanica Solida Sinica 36 (2023) 181–213. doi:https://doi.org/10.1007/s10338-023-00380-5.

[34] C. Liang, Y. Yin, W. Wang, M. Yi, A thermodynamically consistent non-isothermal phase-field model for selective laser sintering, International Journal of Mechanical Sciences 259 (2023) 108602. doi:10.1038/s41524-019-0219-7.

[35] O. S. Carneiro, A. F. Silva, R. Gomes, Fused deposition modeling with polypropylene, Materials and Design 83 (2015) 768–776. doi:10.1016/j.matdes.2015.06.053.

[36] M. Zhou, S. Xu, Y. Li, C. He, T. Jin, K. Wang, H. Deng, Q. Zhang, F. Chen, Q. Fu, Transcrystalline formation and properties of polypropylene on the surface of ramie fiber as induced by shear or dopamine modification, Polymer 55 (2014) 3045–3053. doi:10.1016/j.polymer.2014.05.013.

[37] A. S. Nielsen, R. Pyrz, Study of the influence of thermal history on the load transfer efficiency and fibre failure in carbon/polypropylene microcomposites using raman spectroscopy, Composite Interfaces 6 (1998) 467–482. doi:10.1163/156855499X00152.

[38] X.-D. Wang, J. Ouyang, J. Su, W. Zhou, A phase-field model for simulating various spherulite morphologies of semi-crystalline polymers, Chinese Physics B 22 (10) (2013) 106103. doi:10.1088/1674-1056/22/10/106103.

[39] A. Bahloul, I. Doghri, L. Adam, An enhanced phase field model for the numerical simulation of polymer crystallization, Polymer Crystallization 3 (2020) e10144. doi:10.1002/pcr2.10144.

[40] A. Bahloul, I. Doghri, L. Adam, Linking a phase field model for polymer crystallization to full-field micromechanical simulations of semi-crystalline polymers, Computational Materials Science 199 (2021) 110685. doi:10.1016/j.commatsci.2021.110685.

[41] L. Gránásy, T. Pusztai, G. Tegze, J. A. Warren, J. F. Douglas, Growth and form of spherulites, Physical Review E 72 (1) (2005) 011605. doi:10.1103/PhysRevE.72.011605.

[42] M. Fan, W. He, Q. Li, J. Zhou, J. Shen, W. Chen, Y. Yu, Ptfe crystal growth in composites: A phase-field model simulation study, Materials 15 (2022) 6286. doi:10.3390/ma15186286.

[43] Y. Yang, O. Ragnvaldsen, Y. Bai, M. Yi, B. Xu, 3d non-isothermal phase-field simulation of microstructure evolution during selective laser sintering, npj Computational Materials 5 (81) (2019). doi:10.1038/s41524-019-0219-7.

[44] Z. H. Stachurski, J. MacNicol, The geometry of spherulite boundaries, Polymer 39 (1998) 5717–5724. doi:10.1016/S0032-3861(97)10186-0.

[45] I. Coccorullo, R. Pantani, G. Titomanlio, Crystallization kinetics and solidified structure in ipp under high cooling rates, Polymer 44 (1) (2003) 307–318. doi:10.1016/S0032-3861(02)00762-0.

[46] T. W. Heo, L. Chen, Phase-field modeling of nucleation in solid-state phase transformations, Jom 66 (2014) 1520–1528. doi:10.1007/s11837-014-1033-9.

[47] M. P. Howard, S. T. Milner, A simple model for heterogeneous nucleation of isotactic polypropylene, Macromolecules 46 (16) (2013) 6593–6599. doi:10.1021/ma400702q.

[48] O. Dolynchuk, T. Thurn-Albrecht, On thermodynamics and kinetics of interface-induced crystallization in polymers, Macromolecular Chemistry and Physics (2023) 2200455doi:10.1002/macp.202200455.

[49] C. J. Permann, M. R. Tonks, B. Fromm, D. R. Gaston, Order parameter re-mapping algorithm for 3d phase field model of grain growth using fem, Computational Materials Science 115 (2016) 18–25. doi:10.1016/j.commatsci.2015.12.042.

[50] J. Brandrup, E. H. Immergut, E. A. Grulke, A. Abe, D. R. Bloch, Polymer handbook, Vol. 89, Wiley New York, 1999. doi:10.1002/1097-0126(200007)49:7<807::AID-PI436>3.0.CO;2-1.

[51] L. Girifalco, R. J. Good, A theory for the estimation of surface and interfacial energies. i. derivation and application to interfacial tension, The Journal of Physical Chemistry 61 (7) (1957) 904–909. doi:10.1021/j150553a013.

[52] K.-Y. Law, H. Zhao, Determination of Solid Surface Tension by Contact Angle, Springer International Publishing, Cham, 2016, pp. 135–148. doi:10.1007/978-3-319-25214-8_7.

[53] P. Plastics, Thermal properties of plastic materials, https://www.professionalplastics.com/professionalplastics/ThermalPropertiesofPlasticMaterials.pdf (n.d.).

[54] C. J. Permann, D. R. Gaston, D. Andrš, R. W. Carlsen, F. Kong, A. D. Lindsay, J. M. Miller, J. W. Peterson, A. E. Slaughter, R. H. Stogner, et al., Moose: Enabling massively parallel multiphysics simulation, SoftwareX 11 (2020) 100430. doi:10.1016/j.softx.2020.100430.

[55] J. Magill, A new technique for following rapid rates of crystallization ii isotactic polypropylene, Polymer 3 (1962) 35–42. doi:10.1016/0032-3861(62)90064-2.

[56] A. Włochowicz, M. Eder, Analysis of the crystallization kinetics of isotactic polypropylene by infra-red spectroscopy, Polymer 22 (9) (1981) 1285–1287. doi:10.1016/0032-3861(81)90148-8.

[57] Y. Zhang, V. Shapiro, Linear-time thermal simulation of as-manufactured fused deposition modeling components, Journal of Manufacturing Science and Engineering 140 (7) (2018) 071002. doi:10.1115/1.4039556.

[58] M. Mehdikhani, L. Gorbatikh, I. Verpoest, S. V. Lomov, Voids in fiber-reinforced polymer composites: A review on their formation, characteristics, and effects on mechanical performance, Journal of Composite Materials 53 (12) (2019) 1579–1669. doi:10.1177/0021998318772152.